

Resonant Rayleigh scattering dynamics of excitons in single quantum wells

G. Kocherscheidt, W. Langbein, and U. Woggon

Experimentelle Physik IIb, Universität Dortmund, Otto-Hahn-Strasse 4, 44221 Dortmund, Germany

V. Savona

Institute of Theoretical Physics, Swiss Federal Institute of Technology, Lausanne, CH-1015 Lausanne EPFL, Switzerland

R. Zimmermann

Institut für Physik der Humboldt-Universität zu Berlin, 10117 Berlin, Germany

D. Reuter and A. D. Wieck

Angewandte Festkörperphysik, Ruhr-Universität Bochum, Universitätsstrasse 150, 44780 Bochum, Germany

(Received 3 July 2002; revised manuscript received 16 April 2003; published 26 August 2003)

The resonant Rayleigh scattering dynamics of excitons in single GaAs quantum wells is investigated. The deviation of the measured intensity from the ideal ensemble average is analyzed as a function of the speckle ensemble size. The influence of the amplitude and correlation length of the exciton disorder potential is traced using a series of samples with varying inhomogeneous broadening and interface island sizes. The experimental data are compared with theoretical predictions using exciton states of spatially uncorrelated energies, as well as full calculations of the exciton polarization dynamics using a more realistic disorder potential including the formation of monolayer islands. Deviations from the dynamics of uncorrelated states are found at early times after excitation. They are reproduced by the calculations possessing a state correlation due to quantum mechanical level repulsion and a finite correlation length for the disorder potential. Additionally, the presence of a long-range disorder potential in the micrometer range is suggested. Changing the disorder potential by varying the island size influences the observed dynamics systematically according to the different disorder correlation lengths.

DOI: 10.1103/PhysRevB.68.085207

PACS number(s): 78.67.De, 78.35.+c, 78.47.+p

I. INTRODUCTION

Almost 20 years ago Hegarty *et al.*¹ reported strong resonant light scattering from quantum well (QW) excitons. It was recognized as resonant Rayleigh scattering (RRS), in which static disorder leads to coherent scattering of light in directions other than specular ones. In quantum wells such disorder has its origin in alloy disorder² or in the formation of monolayer islands at the QW interfaces.³ It results in a disorder potential for the spatial motion of the QW excitons in the QW plane, in which they can be localized and act as resonant scatterers. The investigation of RRS from QW excitons can thus give insight in the disorder properties of the underlying material and a growing number of publications in the past few years show the intense research activity in this field.^{4–15}

Recent publications point out two main mechanisms that influence the dynamics of the resonantly scattered light.^{16–19} On one hand a strong influence of the radiative coupling between the different layers of a multiple quantum well (MQW), i.e., a pure polaritonic effect, was reported,¹⁶ leading to strong initial oscillations in the RRS dynamics of MQW's, as opposed to what was observed in single quantum wells (SQW). Such radiative coupling effects are especially strong in Bragg arranged MQW structures, where the RRS dynamics is found to be dominated by the polaritonic modes.¹⁷ On the other hand, the exciton states in a disordered potential show correlations in the energy level statistics due to an interplay of *both* quantum-mechanical level-repulsion,

i.e., a reduction in the probability of finding exciton states close in energy and space, and a finite spatial correlation length of the disorder potential, as was predicted in Ref. 18 and observed using near-field photoluminescence spectroscopy of a thin GaAs SQW.²⁰ These correlations in the level statistics can also lead to temporal oscillations in the RRS dynamics,¹⁸ and observations on MQWs¹⁹ have been interpreted in this way.

To isolate the effect of the in-plane level statistics from polaritonic effects, we investigate in this work the RRS dynamics on a series of SQWs designed for the systematic variation of disorder potential properties. In SQWs the effect of radiative coupling is reduced to a minimum compared to the previously used MQW structures.

II. SAMPLE DESIGN

To discuss the design of the investigated SQW samples, we first introduce the relevant quantity determining the RRS dynamics, which is the effective disorder potential $V(\mathbf{R})$ for the exciton center-of-mass (c.m) motion, where \mathbf{R} denotes the exciton c.m. coordinate.¹⁸ To describe quantities independent of the specific realization, we consider the statistical properties of $V(\mathbf{R})$, which is formed as an average over the exciton relative wave function, covering many crystal unit cells, each randomly occupied in the $\text{Al}_x\text{Ga}_{1-x}\text{As}$ case by either an Al or a Ga atom. It can therefore be modeled by a Gaussian distributed potential, characterized by its amplitude variance σ_v and a spatial correlation function f_C :

$$\langle V(\mathbf{R})V(\mathbf{R}') \rangle = \sigma_v^2 f_C(\mathbf{R} - \mathbf{R}'). \quad (1)$$

The brackets denote the ensemble average, which we assume to be equal to the spatial average over \mathbf{R} . For simplicity, f_C is often considered isotropic and containing only a single correlation length ξ . In literature, Gaussian and exponential f_C have been used.^{18,20} The RRS dynamics in such a potential is characterized by the ratio σ_v/E_c , where E_c is the kinetic energy corresponding to the correlation length ξ with the exciton translational mass M , and is given by $E_c \equiv \hbar^2/(2M\xi^2)$.

In the epitaxial growth of QW structures, two obvious possibilities to affect the properties of the disorder potential are present. First, one can increase the variance σ_v of the disorder potential by decreasing the width L_z of the QW, where σ_v scales roughly like L_z^{-3} when interface roughness is dominating and the wave function penetration into the barrier is negligible. Second, a temporal interruption of the epitaxial growth process at the QW interfaces leads to the formation of large monolayer islands on the surface.²¹ The lateral extent of the islands increases with increasing growth interruption (GI) time, and consequently, extending the correlation length ξ of the created disorder potential. We used both methods to modify the disorder potential in the samples studied. They are GaAs/Al_{0.2}Ga_{0.8}As SQW's and were grown by molecular-beam epitaxy (MBE) on undoped GaAs substrates. First, a 100-nm GaAs buffer layer was grown, followed by a 30-nm Al_{0.2}Ga_{0.8}As barrier layer and the GaAs QW material of different thicknesses. Afterwards a GI was applied, invoking the formation of large monolayer islands on the GaAs surface. This particular growth process can lead to island sizes up to several hundred nanometers³ depending on the GI time. The GaAs islands were overgrown with a 1-nm AlAs layer to maximize the impact of the island formation on the exciton disorder potential. The AlAs layer is followed by a 30-nm Al_{0.2}Ga_{0.8}As barrier layer. Several QWs of different thicknesses are stacked in one sample. The GI is applied only on the top interface of the well in order to create a disorder potential with only one long correlation length. All other disorder, including barrier alloy disorder, segregation of Al into the QW, and the island formation of the lower Al_{0.2}Ga_{0.8}As/GaAs interface, is expected to have a correlation length below the exciton Bohr radius a_B . Thus it affects the c.m. disorder potential that is averaged over the exciton relative wave function similar to a white-noise disorder. Hence, the total disorder potential has a bimodal structure² consisting of one part with the exciton Bohr radius as correlation length, and another part of larger correlation length due to the island formation during the GI. The experimentally realized disorder potential is therefore more complex than theoretical approaches using only one correlation length. Two sets of SQWs were grown in this way: Set A of increasing GI time (5–120 s) with decreasing well width (16–5.4 nm) and set B with a constant, long GI time (120 s) and different well widths (7–30 nm). Additionally, we investigated a set C of SQW's of different thicknesses (9–20 nm) with Al_{0.7}Ga_{0.3}As barriers, without the AlAs layer and the GI. It is expected to exhibit only a short disorder correlation

TABLE I. Properties of the investigated SQW's: Wafers 1–5: different undoped (100) GaAs substrate wafers. MBE 1,2: different MBE growth machines.

Set	L_z (nm)	GI (s)	Wafer	MBE
A	14.9	0	1	1
A	11.2	2	1	1
A	8.3	10	1	1
A	12.9	1	2	1
A	9.7	5	2	1
B	30	120	3	1
B	20	120	3	1
B	15	120	3	1
B	12	120	3	1
B	9	120	3	1
C	20	0	4	2
C	12	0	4	2
C	9	0	4	2
C	25	0	5	2
C	15	0	5	2

length. Details on the distribution of the SQW's onto physically different samples are given in Table I.

III. THEORETICAL MODELING

Before discussing the experimental results, we consider theoretical models to describe the RRS dynamics. The dynamics of uncorrelated exciton states are compared with the results of a calculation of the full polarization dynamics in disorder realizations with statistical properties given by Eq. (1).

A. RRS dynamics of uncorrelated level ensembles

For an ensemble of undamped two-level systems with a homogeneous spatial distribution of oscillator strength, and with energies and oscillator strengths uncorrelated to their spatial positions, the RRS dynamics after short pulse excitation at $t=0$ is determined by the normalized RRS intensity spectrum $p(\omega)$ to be

$$I_{\text{RRS}}(t) \propto 1 - |\tilde{p}(t)|^2, \quad (2)$$

$$\tilde{p}(t) = \int e^{i\omega t} p(\omega) d\omega, \quad \tilde{p}(0) = 1,$$

with $\tilde{p}(t)$ being the Fourier transform of $p(\omega)$. Using this dependency, the expected uncorrelated RRS dynamics for a given measured RRS spectrum can be calculated and compared with the measurements. Deviations between the two give evidence for level correlations in the system. However, exciton states show a microscopic polarization decay due to radiative decay and phonon scattering, in contrast to the assumption of undamped two-level systems. If the RRS spectrum is much broader than the homogeneous broadening, this decay is much slower than the initial RRS dynamics given by Eq. (2), and does not significantly influence the initial

dynamics. However, effects of level correlation, especially level repulsion, can have an energy range comparable to the homogeneous broadening, so that care has to be taken in analyzing the contributions of level statistics and microscopic dephasing.

A specific, analytically treatable example of an uncorrelated level ensemble is used in the Gaussian random level model that was already applied in Refs. 12,13,22. It considers an ensemble of two-level systems with a Gaussian distribution of eigenfrequencies ω of variance σ centered at ω_0 , and equal oscillator strength of all systems, so that we get

$$p(\omega) = \frac{1}{\sigma\sqrt{2\pi}} \exp\left(-\frac{1}{2} \frac{(\omega - \omega_0)^2}{\sigma^2}\right). \quad (3)$$

Interaction of the two-level systems with the environment is introduced in terms of simple damping factors for the diagonal and the off-diagonal elements of the density matrix of each two-level system. The density decay rate $2\gamma_r$ is the diagonal damping (for example, due to radiative decay), and the polarization decay rate γ is the off-diagonal damping. It is given by the pure dephasing rate γ_p (for example, by phonon scattering) and γ_r according to $\gamma = \gamma_p + \gamma_r$. The spatial distribution of dipoles is assumed to be homogeneous within the optically accessible wave-vector range. The two-level systems are excited by a δ pulse at zero time, creating a secondary emission dynamics given by

$$\bar{I} = I_0 e^{-2\gamma_r t} (1 - e^{-2\gamma_p t - \sigma^2 t^2}), \quad (4)$$

$$\bar{I}_{\text{RRS}} = I_0 e^{-2\gamma t} (1 - e^{-\sigma^2 t^2}). \quad (5)$$

B. Microscopic theory

To treat the RRS dynamics of $1s$ excitons in SQW's microscopically, we use the model proposed in Ref. 18, in which only the dynamics of the center-of-mass exciton motion is calculated, while the relative electron-hole motion is assumed to be unaffected by the disorder. This is accurate for in-plane disorder potentials much smaller than the exciton binding energy, as it is the case for the investigated samples. Additionally, polaritonic effects are neglected, which should be a good approximation for SQW's with a disorder bigger than the radiative decay rate of the free exciton $\gamma_{r0} \approx 0.05 \text{ ps}^{-1}$. Within these approximations, the time-dependent exciton polarization in real space $P(\mathbf{R}, t)$ obeys the equation

$$\begin{aligned} & \left(\hbar(\omega_x + i\gamma + i\partial_t) + V(\mathbf{R}) - \frac{\hbar^2}{2M} \Delta_{\mathbf{R}} \right) P(\mathbf{R}, t) \\ & = \mu E_0 \delta(t) e^{i\mathbf{k}_0 \mathbf{R}}, \end{aligned} \quad (6)$$

where $\hbar\omega_x$ is the exciton energy without disorder at $\mathbf{k} = 0$, M is the c.m. exciton mass, and γ is a phenomenological damping constant representing radiative decay and phonon scattering. Using only one damping constant for the polarization in real space is an approximation, since the radiative coupling depends on the in-plane momentum of the polarization, and the phonon scattering at low temperatures depends on the

available final exciton states in real space at lower energies. These effects could be taken into account by solving the exciton motion in the disorder exactly, and calculating the polarization dynamics in the disorder eigenstates.²³ This is, however, beyond the scope of this paper. The effect of the single damping constant γ is an exponential decay of the RRS intensity, which is also observed in the experiments presented later, justifying the usage of a single γ . $E_0 \delta(t) e^{i\mathbf{k}_0 \mathbf{R}}$ is the incoming excitation pulse, a plane wave of short pulse duration, and μ is the dipole matrix element of the excitonic transition. The disorder potential $V_{\mathbf{R}}$ for the exciton c.m. motion results from the variations of the band energies for electron and hole by the random distribution of Ga and Al atoms in the QW region, averaged over the electron-hole relative motion in the $1s$ exciton.²⁴

As discussed before, the microscopic disorder of an MBE-grown GaAs SQW consists of an alloy disorder part with a correlation length below the exciton Bohr radius, and the part due to interface monolayer islands, with a correlation length typically between 5 nm and 500 nm, depending on the growth interruption time at the interfaces. The potential correlation should thus contain several length scales. For a qualitative understanding, we first consider a single correlation length of Gaussian type, as widely applied in literature:¹⁸⁻²⁰

$$f_{\mathbf{C}}(\mathbf{R}) = \exp\left(-\frac{\mathbf{R}^2}{2\xi^2}\right). \quad (7)$$

The polarization equation is solved numerically on an equidistant grid in real space, using periodic boundary conditions. M was chosen to be $0.25m_e$, and $\gamma = 10 \mu\text{eV}$. Typical simulation areas are $1 \mu\text{m}^2$, using 128×128 grid points. The RRS intensity

$$I_{\text{RRS}}(\mathbf{k}, t) \propto \left| \int e^{-i\mathbf{k}\mathbf{R}} P(\mathbf{R}, t) d\mathbf{R} \right|^2 \quad (8)$$

is averaged over 5000 disorder realizations. The excitation is at normal incidence ($\mathbf{k}_0 = 0$), and the RRS intensity is evaluated at $\mathbf{k} \approx 2\pi\mu\text{m}^{-1}$. The resulting spectra of absorption and RRS are shown in Fig. 1 for different correlation lengths ξ and fixed $\sigma_v = 1 \text{ meV}$. With increasing σ_v/E_c , the spectra pass from a slightly asymmetric shape with a high-energy tail and reduced spectral width to a symmetric Gaussian shape of a width given by σ_v . The reduction of the linewidth for small σ_v/E_c is due to averaging over the disorder by the finite extension of the exciton states l_{loc} , also called motional narrowing. In the following, we define σ for a non-Gaussian line shape by its full width at half maximum of $\sigma\sqrt{8 \ln 2}$. Since the exciton motion is two dimensional, the number of averaged independent potential sites can be estimated to be $\propto (l_{\text{loc}}/\xi)^2 \propto E_c/\sigma_v$, so that the resulting widths of the RRS spectra σ and of the absorption σ_{abs} are $\propto \sqrt{E_c/\sigma_v}$. This scaling (dashed line in bottom of Fig. 1) is reproduced by the calculation for $\sigma_v/E_c \ll 1$, as expected. In the whole range of σ_v/E_c , we find the interpolation

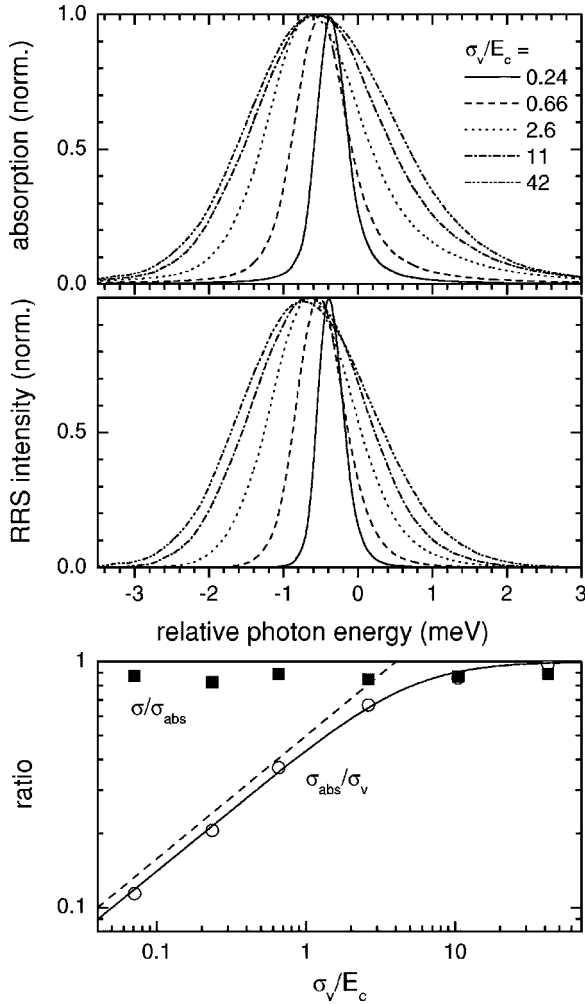


FIG. 1. Calculated spectra of the absorption (top) and RRS intensity (middle) versus the photon energy relative to $\hbar\omega_x$ for different ratios σ_v/E_c as indicated, for a single Gaussian correlation of the disorder potential [Eq. (7)], and for $\sigma_v=1$ meV and $\gamma=10$ μ eV. Bottom: Resulting width of the absorption relative to the potential variance $\sigma_{\text{abs}}/\sigma_v$ (circles), and width of the RRS intensity relative to σ_{abs} , $\sigma/\sigma_{\text{abs}}$ (squares), versus σ_v/E_c . The dashed line indicates the scaling behavior $\sqrt{E_c/\sigma_v}$. The solid line is an interpolation according to Eq. (9).

$$\frac{\sigma_{\text{abs}}}{\sigma_v} \approx \left[1 + \left(\frac{5E_c}{\sigma_v} \right)^{3/2} \right]^{-1/3} \quad (9)$$

and $\sigma \approx 0.85\sigma_{\text{abs}}$.

Only the initial dynamics of the RRS is affected by the level statistics, while after a long time all exciton states have random relative phases, so that the RRS is decaying like the microscopic polarization of the excitons states, which is γ in our model. In order to concentrate on the effects of level statistics, we show the RRS dynamics for $\gamma=0$, and normalize the calculated RRS to its long-time intensity level. It was shown that the RRS dynamics on the dimensionless time scale $\sigma_v t$ is determined by the ratio σ_v/E_c . Since the uncorrelated RRS dynamics is determined by σ , which is directly accessible in the experiment, we display the RRS dynamics versus the time scale σt instead of $\sigma_v t$. The calculated RRS

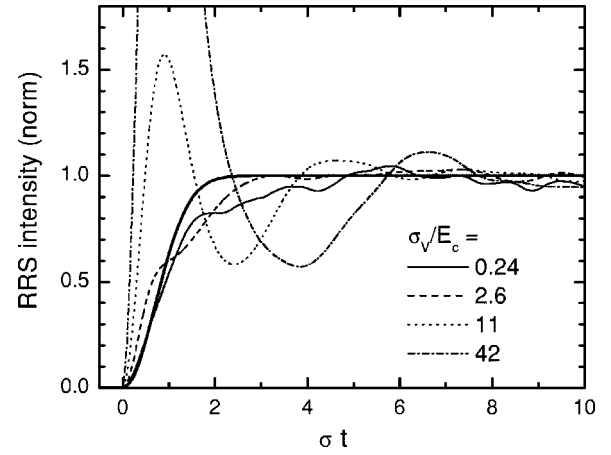


FIG. 2. Calculated RRS intensity versus reduced time σt after excitation, for different values of σ_v/E_c as indicated, and $\gamma=0$. The RRS intensity is normalized at long times. The thick solid curve is the uncorrelated RRS dynamics of Eq. (5).

dynamics for different correlation lengths ξ and fixed $\sigma_v=1$ meV are given in Fig. 2 for $\gamma=0$. For $\sigma_v/E_c < 1$, the quantum-mechanical level-repulsion effect dominates the level statistics, which leads to an initial reduction of the RRS intensity, slowly recovering to the uncorrelated response due to the small energy range of strong level repulsion.¹⁸ For $\sigma_v/E_c \gg 1$, the long-range spatial potential correlation leads to an initially increased RRS intensity due to the super-radiance of excitons within one correlation length, which decays to the long-time value with a strongly damped oscillation.

Having discussed the case of a single correlation length, we now turn to a disorder potential more adapted to model the situation of MBE-grown samples, $V=V_{\text{ml}}+V_{\text{sr}}$, the sum of a monolayer potential V_{ml} , and a short-range correlated potential V_{sr} . V_{sr} represents the short-range atomistic disorder, averaged by the exciton relative wave function. We therefore represent it by averaging of a spatially uncorrelated Gaussian function over an exponential weight function $\exp(-|\mathbf{R}-\mathbf{R}'|/\xi_{\text{sr}})$, where the correlation length ξ_{sr} is similar to the exciton Bohr radius; we use $\xi_{\text{sr}}=10$ nm. The resulting potential V_{sr} has the spatial correlation f_e , and the variance σ_{sr} :

$$\langle V_{\text{sr}}(\mathbf{R})V_{\text{sr}}(\mathbf{R}') \rangle = \sigma_{\text{sr}}^2 f_e(\mathbf{R}'-\mathbf{R}) \quad (10)$$

$$f_e(\Delta\mathbf{R}) = \frac{2}{\pi\xi_{\text{sr}}^2} \int \exp\left(-\frac{|\mathbf{R}|+|\mathbf{R}+\Delta\mathbf{R}|}{\xi_{\text{sr}}}\right) d\mathbf{R}.$$

The monolayer potential V_{ml} considers two monolayers of equal surface coverage, separated by the energy σ_{ml} . The spatial distribution of the monolayers is created using a flooding model of a Gaussian correlated random potential v .

$$V_{\text{ml}}(\mathbf{R}) = \frac{\sigma_{\text{ml}}}{2} \text{sgn}[v(\mathbf{R})],$$

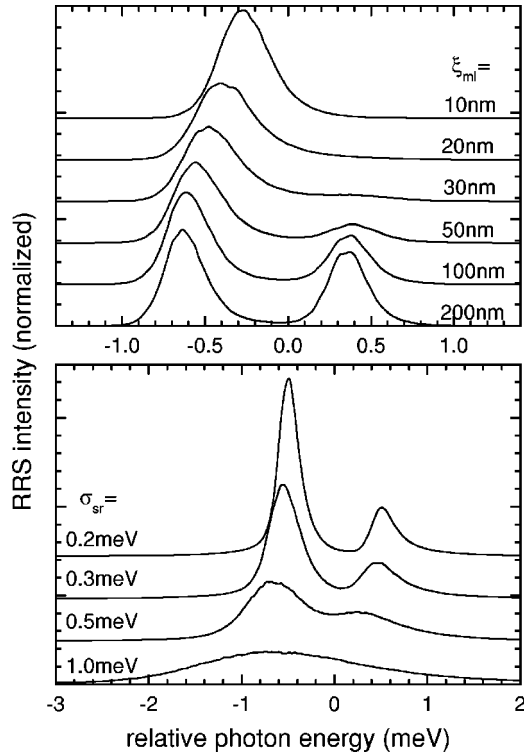


FIG. 3. Calculated spectra of the RRS intensity for a monolayer splitting of 1 meV and $\gamma = 10 \mu\text{eV}$. Top: Fixed $\sigma_{\text{sr}} = 0.3 \text{ meV}$ and different correlation lengths ξ_{ml} of the monolayer potential as indicated. Bottom: Fixed $\xi_{\text{ml}} = 50 \text{ nm}$ and different short-range potential variance σ_{sr} as indicated.

$$\langle v(\mathbf{R})v(\mathbf{R}') \rangle = \exp\left(-\frac{|\mathbf{R}' - \mathbf{R}|^2}{2\xi_{\text{ml}}^2}\right). \quad (11)$$

We have chosen a fixed monolayer splitting $\sigma_{\text{ml}} = 1 \text{ meV}$ in the following simulations, which is realistic for a GaAs quantum well of about 13 nm width.³ We first study the influence of the monolayer correlation length ξ_{ml} for a fixed $\sigma_{\text{sr}} = 0.3 \text{ meV}$. The simulated RRS spectra are shown at the top of Fig. 3. The monolayer splitting begins to appear in the RRS spectra for $\xi_{\text{ml}} = 30 \text{ nm}$, and is fully developed at 100 nm. At 200 nm, both monolayer peaks are nearly equally strong, indicating a full localization of the excitons within one monolayer island by V_{sr} .

The corresponding RRS dynamics are given in Fig. 4 (solid curves), together with the uncorrelated dynamics (dashed curves) deduced from the calculated RRS spectra. The dependence of the dynamics on ξ_{ml} is similar to the results of the single correlation length (Fig. 2), going from a level-repulsion-dominated slow rise for small ξ_{ml} to an initial increase of the RRS by the spatial potential correlation for large ξ_{ml} . Additionally, oscillations corresponding to the monolayer splitting energy are superimposed, which are strongly damped with time. The comparison with the uncorrelated dynamics shows that the oscillations due to the monolayer splitting are significantly enhanced by the level statistics. Note also that the initial RRS enhancement de-

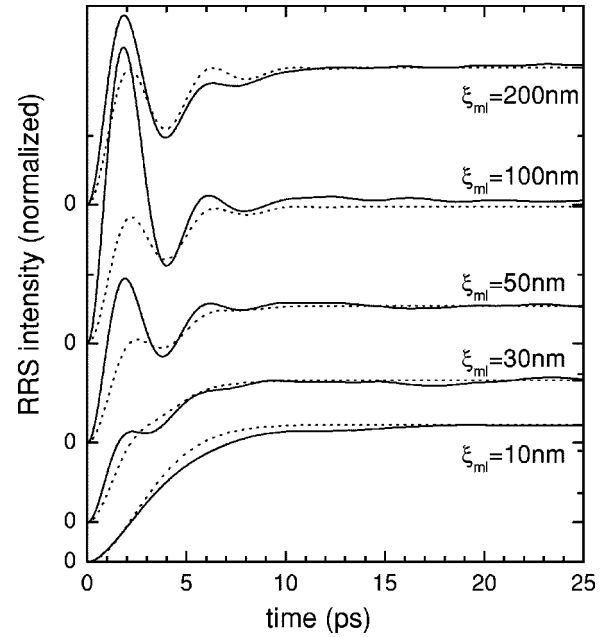


FIG. 4. Calculated time-resolved RRS intensity, for different ξ_{ml} as indicated, $\sigma_{\text{sr}} = 0.3 \text{ meV}$, and $\gamma = 0$. The RRS intensity is normalized at long times. The dashed curves are the uncorrelated RRS dynamics deduced from the calculated RRS spectrum using Eq. (2).

creases as ξ_{ml} goes from 100 nm to 200 nm, opposite to what would be expected from a single correlation length (Fig. 2). This is a direct consequence of the two disorder contributions: If the monolayer islands are large enough that excitons get localized inside without being influenced by the monolayer island borders, the energy levels of the two monolayers are uncorrelated and the RRS dynamics is an uncorrelated sum of the response of two systems of fixed monolayer height with only the short-range potential.

The dependence of the RRS on the short-range disorder σ_{sr} for a fixed monolayer correlation length $\xi_{\text{ml}} = 50 \text{ nm}$ is shown in the spectra in the bottom of Fig. 3 and the RRS dynamics in Fig. 5. For small σ_{sr} , the monolayer splitting results in two distinct resonances in the spectra, and the RRS dynamics shows a long-lasting oscillation, with an amplitude increased by the level correlation. Increasing σ_{sr} , the RRS dynamics goes gradually to a response dominated by the short-range potential, in agreement with the vanishing monolayer splitting in the RRS spectra.

The RRS dynamics of GI QWs showing a pronounced monolayer splitting in the case of excitation of only one monolayer peak was investigated in Ref. 25. The spatially nonuniform distribution of the oscillator strength of such a partly excited exciton resonance leads to an instantaneous part of the RRS dynamics. In this case, the uncorrelated dynamics is not given by Eq. (2) since the condition of spatially homogeneously distributed resonances is not fulfilled.

To conclude this section of RRS simulations, we stress that as long as the monolayer splitting is not visible in the RRS spectrum, the RRS dynamics is similar to one with a single effective correlation length. Once monolayer splitting

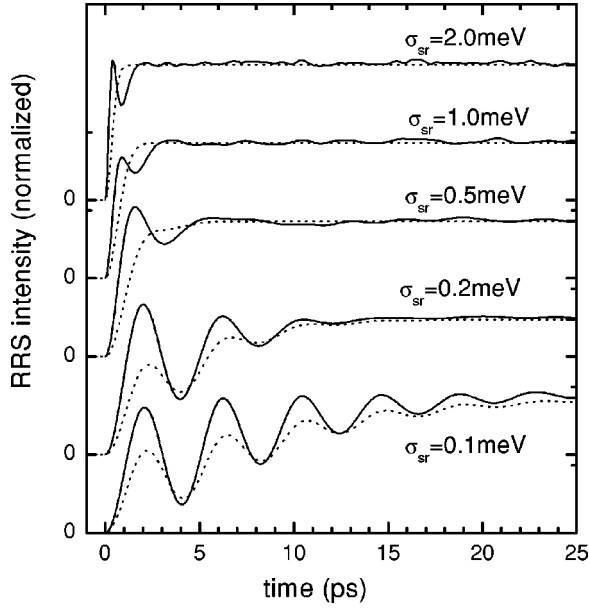


FIG. 5. As Fig. 4, but for different σ_{sr} as indicated, and $\xi_{ml} = 50$ nm.

is observed, the splitting determines the oscillation period of the RRS dynamics, with an oscillation amplitude increased by the level correlation.

IV. EXPERIMENTAL RESULTS AND DISCUSSION

In this section we describe the experiment and present and discuss the experimental results for the RRS dynamics.

A. Experimental details

The samples were placed in a helium cryostat and kept at a temperature of 5 K. The fundamental $hh1-e1$ 1s exciton resonance was resonantly excited p -polarized in the Brewster angle direction by optical laser pulses from a mode-locked Ti:sapphire laser of 500 fs to 2 ps duration. The secondary emission (SE) normal to the sample in the directional range of 0.15 NA was imaged by a sequence of five lenses into a monochromator and its intensity was detected time, energy, and directionally resolved by a synchroscan streak camera. The energy resolution of the Czerny-Turner-type monochromator was adjusted by an aperture on the collimation mirror to about 2 meV. This is small enough to isolate the signal of the resonantly excited SQW from the one of the substrate or other QW's, but also large enough to not reduce the temporal resolution of the streak camera of 2.5 ps. Using the second dimension of the streak camera, the RRS dynamics can be directionally resolved in one dimension, resulting in the parallel detection of about 100 independent RRS intensities (speckles). Repeated measurements of displaced one-dimensional cuts of the two-dimensional directional RRS allowed for the detection of several thousand speckles, a prerequisite to obtain small statistical errors of the deduced speckle averages.

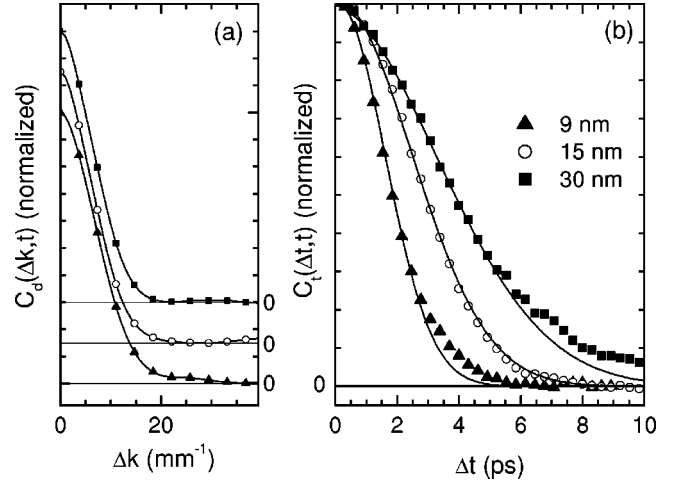


FIG. 6. Correlation functions in time and angular direction for different SQW's of set B, as labeled. (a) Angular correlation $C_d(\Delta k, t)$ for $t = 10$ ps. The curves are vertically displaced for clarity. (b) Time correlation $C_t(\Delta t, t)$ for $t = 10$ ps. The solid lines are the results of the Gaussian uncorrelated model [Eq. (14)] where σ has been fitted to the data.

B. Speckle correlation and analysis

The coherent nature of RRS leads to the formation of speckles in the directional and temporal domain. While the directional extent is given by the spot size, the temporal extent is inversely proportional to the inhomogeneous broadening.

The average directional extent of a speckle can be quantified by the directional correlation $C_d(\Delta \mathbf{k}, t)$ of the directionally and time-resolved secondary emission intensity $I(\mathbf{k}, t)$:

$$C_d(\Delta \mathbf{k}, t) \equiv \frac{\overline{I(\mathbf{k}, t)I(\mathbf{k} + \Delta \mathbf{k}, t)}}{\overline{I(\mathbf{k}, t)} \cdot \overline{I(\mathbf{k} + \Delta \mathbf{k}, t)}} - 1, \quad (12)$$

where the average is taken over the direction identified by the in-plane wave vector \mathbf{k} of the emitted light. For spot sizes much larger than the largest relevant correlation length of the system, this is equivalent to an ensemble average over statistically independent disorder realizations. In Fig. 6(a) the measured $C_d(\Delta \mathbf{k}, t)$ are displayed for three different SQW's. Their full width at half maximum (FWHM) in $\Delta \mathbf{k}$, which quantifies the directional speckle size, is 13 ± 1 mm^{-1} , independent of the time t , and in good agreement with the theoretically expected value of 10 mm^{-1} given by the Gaussian spot size of 380 μm FWHM and the wavelength of $\lambda = 800$ nm when taking into account the directional resolution of the detection of 8 mm^{-1} . The spot size was experimentally determined using a direct imaging of the emission from the sample surface.

The temporal extent of a speckle is quantified by the temporal correlation function $C_t(t, \Delta t)$:

$$C_t(t, \Delta t) \equiv \frac{\overline{I(\mathbf{k}, t)I(\mathbf{k}, t + \Delta t)}}{\overline{I(\mathbf{k}, t)} \cdot \overline{I(\mathbf{k}, t + \Delta t)}} - 1. \quad (13)$$

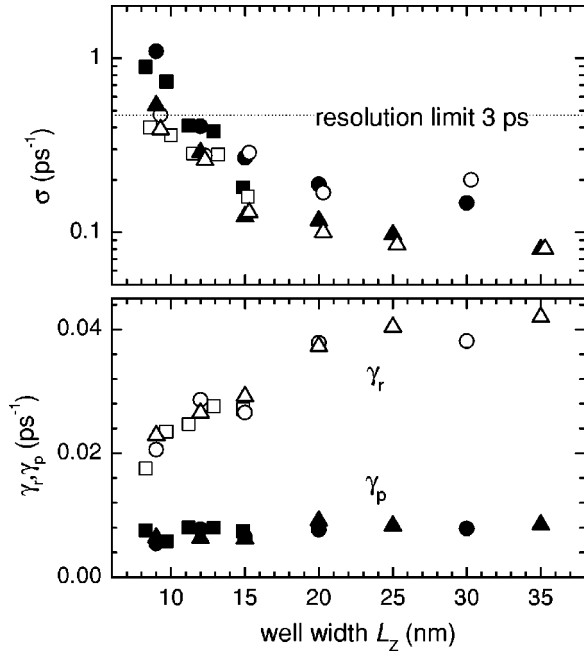


FIG. 7. Parameters of the Gaussian uncorrelated model extracted from the experimental data versus QW width L_z (squares: set A, circles: set B, triangles: set C). Top: σ taken from the RRS spectrum (filled symbols), and extracted from the temporal speckle correlation $C_t(\Delta t, t)$ (open symbols). Bottom: γ_r (open symbols) and γ_p (closed symbols).

In Fig. 6(b) $C_t(t, \Delta t)$ is displayed for the same SQW's as in (a) and $t=10$ ps. Its width in Δt decreases with growing inhomogeneous broadening. The Gaussian uncorrelated model predicts for $\sigma t \gg 1$:

$$C_t(t, \Delta t) = \exp[-\sigma^2 \Delta t^2 - 2\gamma_p(2t + \Delta t)]. \quad (14)$$

The resulting curves (solid lines in Fig. 6) are in agreement with the experiment. For each SQW, we evaluate the pure dephasing γ_p from the dependence of the measured C_t on t , and σ from the dependence on Δt . The density decay rate $2\gamma_r$ is taken from the decay of the secondary emission intensity using Eq. (4). The resulting values at $T=5$ K are displayed in Fig. 7. In the range not limited by the time resolution of the detection, the deduced values of σ (open symbols) are in agreement with the corresponding ones derived from the RRS spectra (filled symbols). The radiative decay rate is decreasing with increasing inhomogeneous broadening, as expected by the decreasing extension of the exciton disorder eigenstates. The pure dephasing rates, which are due to phonon scattering, are $5-10 \text{ ns}^{-1}$, much smaller than the radiative rates, and are nearly independent of QW width.

Before we further analyze the RRS dynamics, we want to discuss the influence of the finite speckle ensemble on the experimental data. In Fig. 8 we show \bar{I} of a 15-nm SQW with 120-s GI for different speckle ensemble sizes n . It is evident that for speckle ensembles with $n < 300$, the temporal speckle fluctuations significantly modify the observed dynamics. To give a quantitative measure for the fluctuations, we derived the standard deviation σ_F of $F = \bar{I}(n)/\bar{I}(\infty)$,

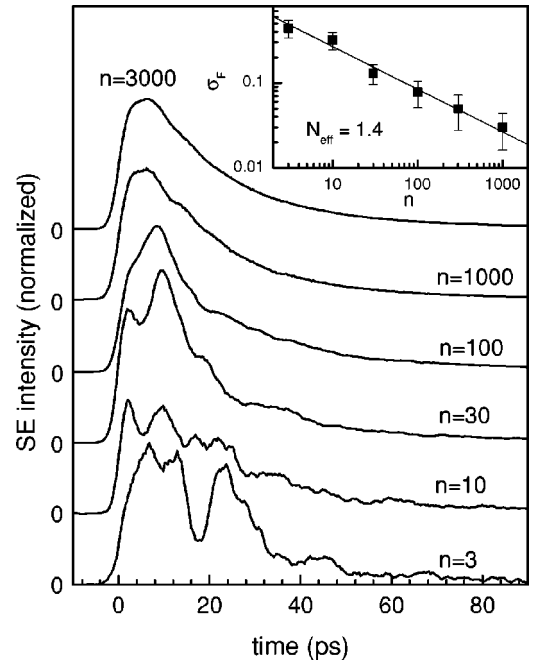


FIG. 8. SE signal of the 15-nm SQW in set B for three different sizes of the speckle ensemble. The curves are vertically displaced for clarity. The inset shows the standard deviation σ_F of the intensity fluctuations, the solid line represents the relation $\sigma_F = (\sqrt{N_{\text{eff}} n})^{-1}$.

where the statistical evaluation is made over the time range 10–40 ps and over different speckle ensembles. The intensity $\bar{I}(\infty)$ for an infinitely large ensemble size was approximated by the largest available average of $n=3000$. The speckle fluctuations reduce with increasing ensemble size, as can be seen in the standard deviation σ_F shown in the inset of Fig. 8. The full line in the inset represents the $1/\sqrt{N_{\text{eff}} n}$ law for a Gaussian distribution of the fluctuations and a fully coherent emission. The experimental data for σ_F is in agreement with the theoretical expectation, and thus the amplitude of the statistical fluctuations can be estimated using this relationship.

Using time-resolved speckle analysis,²² the average RRS intensity $\bar{I}_{\text{RRS}}(t)$ is deduced from the total SE intensity $\bar{I}(t) = \bar{I}_{\text{RRS}}(t) + \bar{I}_{\text{PL}}(t)$, which also includes the incoherent photoluminescence (PL). The coherence degree $c(t) = \bar{I}_{\text{RRS}}/\bar{I}$ is given by $c(t) = \sqrt{N_{\text{eff}} C_t(t, 0)}$, where N_{eff} models the finite temporal and directional resolution of the experiment and represents the number of independent statistical contributions within the experimental resolution.^{12,26} It can be calculated from the statistical properties of $I(t, \mathbf{k})$ ²⁷ and it is in the range $N_{\text{eff}} = 1.2-1.8$ for the experiments shown in this work. Sample results for this analysis shown in Fig. 9 are indicated by symbols. In order to reduce the error of $\bar{I}_{\text{RRS}}(t)$ created by the statistical error of $c(t)$, one can exploit the fact that the incoherent $\bar{I}_{\text{PL}}(t)$ does not show temporal speckle fluctuations, and thus should have a smooth time dependence. We therefore fit the deduced \bar{I}_{PL} with a dynamics given by an exponential rise and an exponential decay, and use the result $I_{\text{PL,fit}}(t)$ to calculate the average

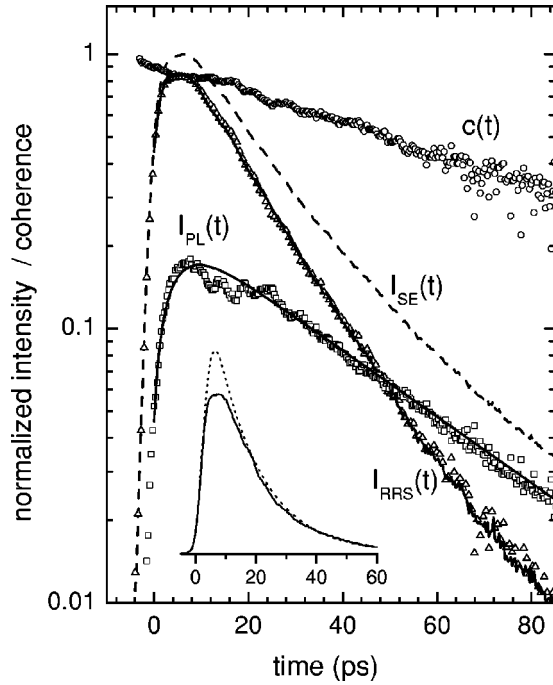


FIG. 9. Time-resolved secondary emission from the 15-nm SQW of set B, and its analysis. SE intensity $\bar{I}(t)$ (dashed line), coherence degree $c(t)$ (circles), coherent intensity \bar{I}_{RRS} (triangles), incoherent intensity \bar{I}_{PL} (squares), its fit $I_{\text{PL,fit}}$ (solid line), and the deduced $I_{\text{RRS,fit}}$ (solid line). The inset shows the comparison between \bar{I}_{RRS} (solid line) and the prediction for uncorrelated levels statistics (dotted) after Eq. (2).

RRS intensity $I_{\text{RRS,fit}}(t) = \bar{I}(t) - I_{\text{PL,fit}}(t)$. The results of this fitting procedure are shown as solid lines in Fig. 9. In the following analysis we use the deduced RRS intensity $I_{\text{RRS,fit}}$.

C. RRS dynamics

The RRS dynamics is determined by two mechanisms: (i) the energy-level statistics, determining the interference between the emission from individual states and (ii) the polarization decay of the individual states due to microscopic scattering processes. In a simple view, the latter process should lead to a superimposed monotonic decay of the RRS intensity, eventually showing a distribution of time constants, and thus a slowing down with time. However, since in general the microscopic dephasing depends on the individual state and its environment, the dephasing rate and the local level statistics are correlated, which could lead to a nontrivial influence on the RRS dynamics. Up to now, this effect has been neglected in simulations of the RRS dynamics. Instead, a single polarization decay rate γ was used, as we also adapted in Eq. (6). The validity of this approximation is supported by the observed exponential decay of $I_{\text{RRS}}(t)$ for intermediate times (typically, $t=20\text{--}50$ ps) over more than one order of magnitude of intensity. We take this decay to determine the total polarization decay rate γ using Eq. (5), since the dynamics due to level statistics is constant at longer

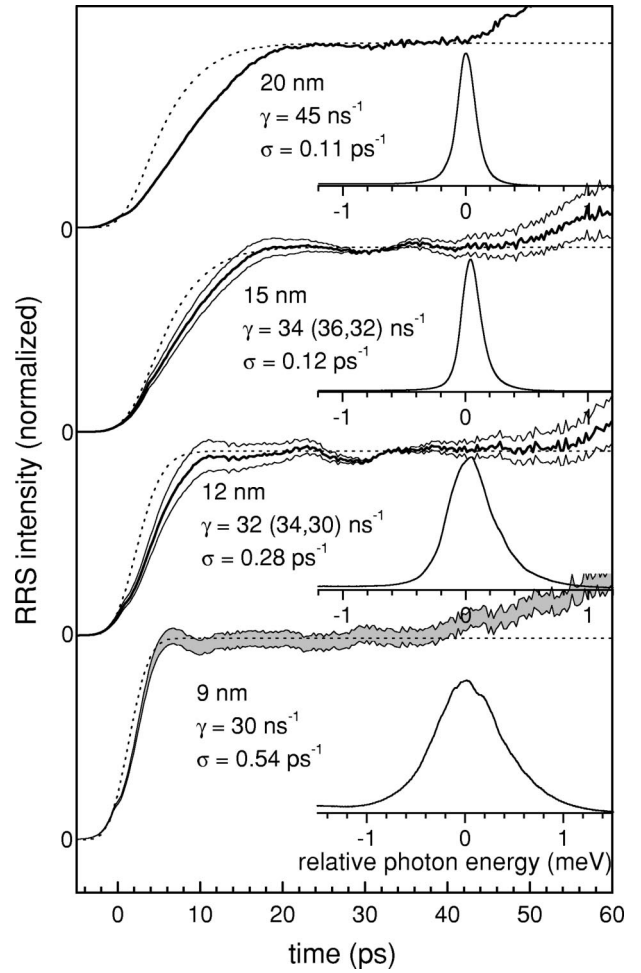


FIG. 10. Decay corrected RRS intensity $\bar{I}_{\text{RRS,dc}}(t)$ (solid) as a function of time, compared with the dynamics deduced from the SE spectrum for uncorrelated level statistics using Eq. (2) (dotted). The different SQW's (set C) of thicknesses as labeled were grown without GI. The insets show the corresponding SE spectra with a resolution of $16 \mu\text{eV}$. The statistical error σ_F of the data is 3.8%, and is visualized ($\pm \sigma_F$) at the data of the 9-nm SQW. The influence of the choice of different γ for decay correction is exemplified for the 15-nm and 12-nm SQW.

times. A distribution of decay rates leads to a gradual decrease of the decay rate with time, which is also found as discussed later.

To compare the impact of the level statistics on the RRS dynamics with the theoretical predictions, we compensate for the average polarization decay γ in the corrected RRS intensity $I_{\text{RRS,cd}}(t) = I_{\text{RRS,fit}}(t) \exp(2\gamma t)$ shown in Figs. 10–12 for the investigated three sets of SQW's. The measured SE spectra are shown in an inset for each SQW. The value of γ is chosen so that the RRS reaches a constant level at intermediate times, and increases towards later times due to the distribution of decay rates. Even though the resulting γ is defined by this requirement to better than 5% accuracy, the resulting RRS dynamics acquires some arbitrariness by the specific choice of γ , which affects the intermediate time dynamics. To exemplify this, the RRS dynamics of the 15-nm and 12-nm SQW of set C is given for three different choices

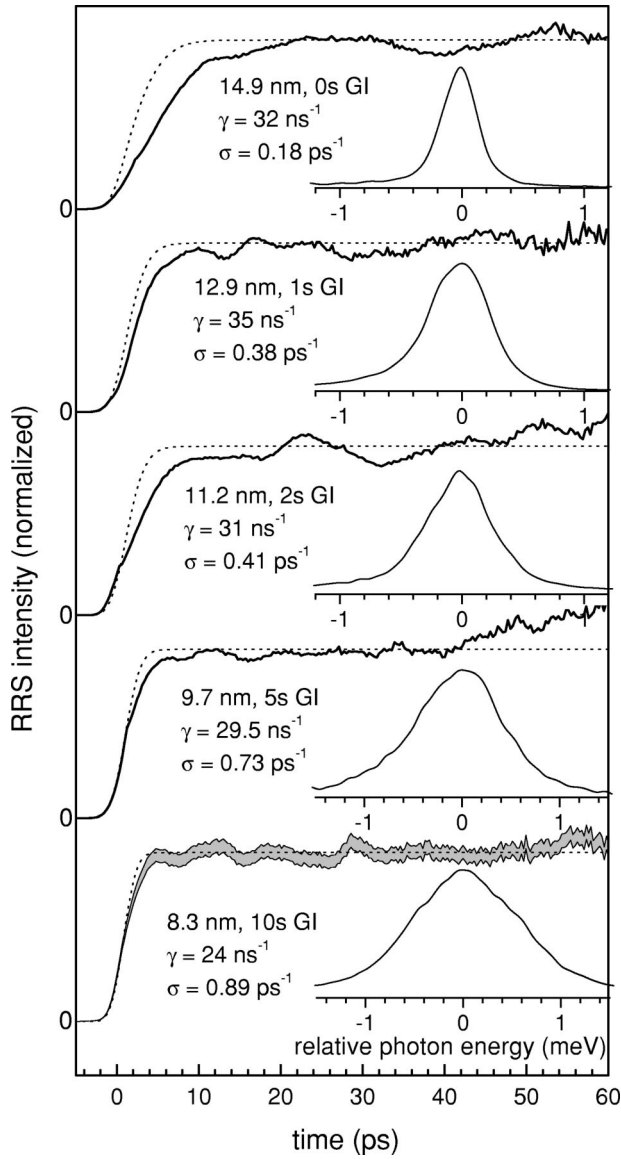


FIG. 11. Same as Fig. 10, but for the SQW set A, with GI duration and thicknesses as indicated. The SE spectra have a spectral resolution of $121 \mu\text{eV}$. The statistical error σ_F of the data is 3.8%, and is visualized ($\pm \sigma_F$) around the data of the 8.3-nm SQW.

of γ (see Fig. 10). One should keep this in mind for the subsequent analysis. Effects of the level statistics on the measured RRS dynamics in the form of pronounced oscillations, which in similar measurements on MQW samples had been assigned to level statistics effects,¹⁹ are absent in the present SQW case. To extract the remaining effects of level statistics, we compare the measured dynamics with the dynamics of an uncorrelated level ensemble having a RRS spectrum that is equal to the measured one [see Eq. (2)], convoluted with the experimental time resolution (dotted lines). Deviations between measurement and prediction are then due to the presence of correlations in the level statistics or due to a distribution of polarization decay rates $p(\gamma)$ within the exciton states.

The measured RRS intensity is lower than the expected uncorrelated dynamics at early times for nearly all SQW's,

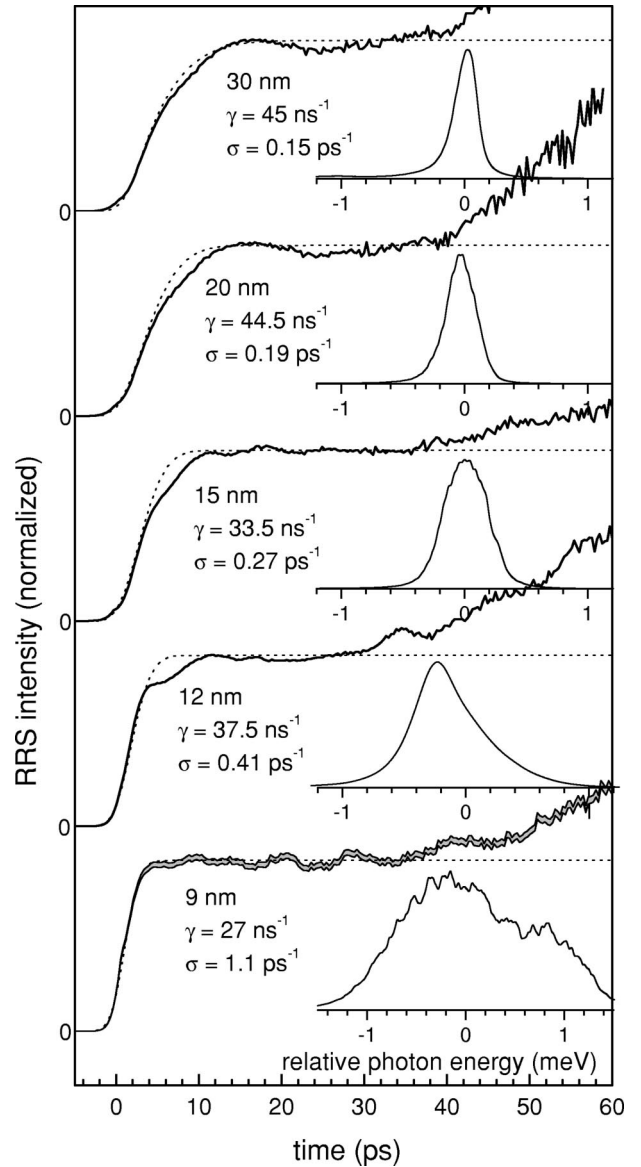


FIG. 12. Same as Fig. 10, but for set B of SQW's with a GI of 120 s and thicknesses as indicated. The SE spectra have a spectral resolution of $16 \mu\text{eV}$. The statistical error σ_F of the data is 1.5%, and is visualized ($\pm \sigma_F$) around the data of the 9-nm SQW.

while in an intermediate time range a rather good agreement is found, i.e., the RRS dynamics becomes exponential. The inset of Fig. 9 illustrates the initial reduction for the 15-nm SQW of set B, where the measured RRS intensity is directly compared with the predicted uncorrelated dynamics, skipping intentionally the PL fit procedure and the decay compensation. The effect of level statistics is also visible in this direct comparison, and is not an artifact of the analysis. A finite width of $p(\gamma)$ leads to a slowing down of the decay with time, i.e., to a positive curvature of the corrected RRS intensity with time. This is actually observed at longer times (> 50 ps), showing that a distribution towards smaller decay rates is present in the investigated samples. Its influence on the initial dynamics would be relevant if a significant part of $p(\gamma)$ would be present at rates larger than the inhomogeneous broadening ($\gamma > \sigma$). At the low lattice temperatures at

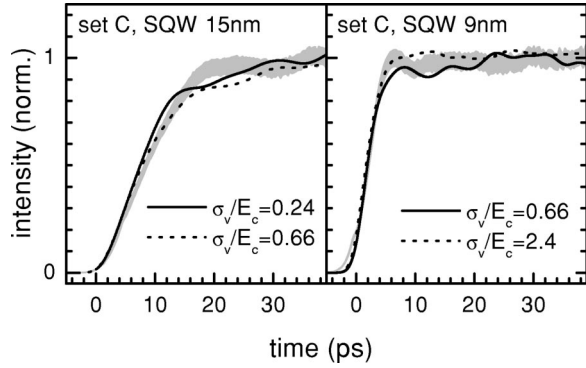


FIG. 13. Comparison of the measured RRS dynamics of the 15-nm and 9-nm SQW of set C (gray shaded region) with the ones calculated for a single disorder correlation length of different σ_v/E_c , convoluted with the experimental time resolution.

which the experiments were conducted, the polarization decay is due to radiative coupling and phonon emission. The radiative rate is always less than $\gamma_{r0} \approx 0.05 \text{ ps}^{-1}$ of the free exciton²⁸ due to the localization of the exciton states. It is thus much less than σ in most of the investigated samples. The phonon emission rate within the rather small ($\leq 1 \text{ meV}$) inhomogeneous broadening of the investigated transitions is calculated to be weaker than the radiative rate.²⁸ These expectations are in agreement with the measured average values of γ_r and γ_p displayed in Fig. 7. In the following, we therefore do not consider the influence of $p(\gamma)$ on the measured initial dynamics.

The initial deviations between measured and uncorrelated dynamics is varying between the samples. We now discuss interpretations of these deviations based on the simulations in the preceding section.

We first consider the samples in which we expect the disorder potential to exhibit only a short correlation length, i.e., set C and a part of set A with short GI times. We compare their response with the theory of only one correlation length [Eq. (7)] using the parameter σ determined from the SE spectra given in Figs. 10 and 11. The calculated dynamics (see Fig. 3), convoluted with the experimental time resolution, is displayed in Fig. 13, together with the measured dynamics of the 15-nm and 9-nm SQW's of set C. Agreement between experiment and calculation is found for $\sigma_v/E_c = 0.24, 0.66$ in the 15-nm case, and for $\sigma_v/E_c = 0.66, 2.6$ in the 9-nm case. For larger values of σ_v/E_c , the calculation deviates significantly from the experiment in both cases. These results are consistent with the values of σ_v/E_c estimated using the structural parameters of the samples: The relationship between σ and σ_v depends on the disorder correlation length ξ , as shown in Fig. 2. A lower limit for ξ is given by the exciton Bohr radius a_B , for which $E_c = 1.4 \text{ meV}$ using $\xi = 10 \text{ nm} \approx a_B$ and $M = 0.25 m_e$. In the considered samples, the disorder correlation length is expected to be short, so that $E_c \approx 1.4 \text{ meV}$. Using the measured values of σ , we estimate σ_v/E_c to be 0.08 (0.36) for the 9-nm (15-nm) SQW. With Eq. (9) the corresponding value of σ_v/E_c is 0.36 (0.95), in quantitative agreement with the value range determined from the measured dynamics. For the

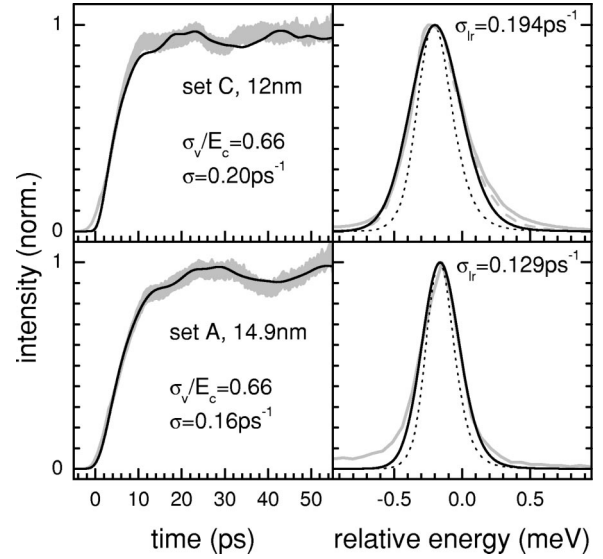


FIG. 14. Left: Comparison of the measured RRS dynamics of the 12-nm SQW of set C and 14.9-nm SQW of set A (gray shaded regions) with the one calculated for a single disorder correlation length of $\sigma_v/E_c = 0.66$ and σ as labeled, convoluted with the experimental time resolution. Right: Measured SE (gray solid line) and RRS (gray dashed line) spectra, compared with the calculated spectra without long-range disorder (dotted lines) and with long-range disorder (solid line) of variance σ_{lr} as indicated.

considered samples, the dynamics is thus described by the prediction of Eq. (6) with a disorder of a correlation length shorter than the exciton Bohr radius.

For some samples, e.g., the 12-nm SQW of set C, this comparison does not result in an agreement for any value of σ_v/E_c ; the measured dynamics is significantly slower than the calculated one. This also holds true when comparing with the model including monolayer islands (see Figs. 4 and 5). The deviation can instead be explained assuming the presence of an additional disorder potential V_{lr} with a correlation length ξ_{lr} larger than the light wavelength, so that the RRS from uncorrelated regions of V_{lr} are interfering with each other with random phases (in the spatial average) for emission wave vectors differing by more than ξ_{lr}^{-1} from the specular direction. The presence of such a long-range component of the disorder potential was also suggested by the observation of initial forward scattering,²⁹ and by the strong scattering angle dependence of the RRS in multiple quantum wells.¹⁶ Recently, also a direct observation of a long-range disorder in GaAs QW's was reported.³⁰ V_{lr} does not change the RRS dynamics except for the wave-vector region around the specular direction. It increases, however, the spectral width of the RRS, since the RRS spectrum is given by the convolution of the spectrum without long-range disorder with the distribution of V_{lr} . We assume the distribution of V_{lr} to be Gaussian with variance σ_{lr} . Having this additional free parameter, we determine σ and σ_v/E_c from the measured RRS dynamics. The long-range disorder width σ_{lr} is then fixed by the RRS spectrum deduced from the SE by spectral speckle analysis.²³ Results of this procedure are shown in Fig. 14 for the 12-nm SQW of set C and the 14.9-nm SQW

of set A. Agreement between calculation and experiment is reached, determining the variance of the long-range disorder σ_{lr} to the values given in the figure, which are quantitatively comparable with results of a direct spatial measurement on similar structures.³⁰ The deduced inhomogeneous broadenings due to long-range and short-range disorder, σ_{lr} and σ_{sr} , are in this example of similar magnitude. The value of $\sigma_v/E_c=0.66$ is consistent with the values of 0.4 and 0.34, deduced from σ and $E_c=1.4$ meV.

The microscopic origin of the long-range disorder is not understood. However, it shows the following systematic behavior: (i) Its relevance decreases with decreasing well width, i.e., its strength seems independent of well width, while the shorter-range disorder potential strength increases with decreasing well width. (ii) It is varying between SQW's grown on different substrates (see Table I). A possible origin could thus be the presence of strain fluctuations by impurities or dislocations.

We now turn to the samples grown with a long growth interruption (set B). Their SE spectra are influenced by the islands of long correlation length on the growth-interrupted GaAs surface. In general, it leads to an increased inhomogeneous broadening (see Fig. 7) compared to similar structures without growth interruption due to the reduced spatial averaging of the spatial disorder by the exciton. Additionally, for well widths below 15 nm, the development of a monolayer splitting starts to be appreciable. This is expected, since the lateral localization length of an exciton due to a monolayer island is decreasing with decreasing well width by the increasing change of the exciton quantization energy at a monolayer step.³¹ This effect can be also seen in Fig. 3, where with increasing correlation length at fixed monolayer quantization energy the monolayer splitting develops. For the 9 nm SQW, the inhomogeneous broadening is too large for the corresponding dynamics to be resolved with our experimental time resolution. Therefore, we have chosen the 12-nm SQW for the comparison with theory. Its SE spectrum shows a pronounced asymmetry to the high-energy side compared to other non growth-interrupted wells of similar thickness. The RRS dynamics is compared in Fig. 15 with the calculated dynamics using the monolayer disorder [Eqs. (11) and (10)]. Agreement of both RRS dynamics and spectra is reached using $\sigma_{sr}=0.18$ meV, $\sigma_{ml}=0.6$ meV, $\xi_{ml}=56$ nm, and $\sigma_{lr}=0.23$ ps⁻¹. σ_{lr} is comparable to the one observed in the 12 nm SQW of set C, and also similar to the long range potential measured in a 11 nm SQW.³⁰ The value of σ_{ml} can be compared with the estimated change of the exciton transition energy within one monolayer step. Using the exciton transition energies E_x of the samples in set B of different thickness L_z , we can estimate $\sigma_{ml}\approx 0.28$ nm $\cdot\partial E_x/\partial L_z$, which results for the 12-nm SQW in 1.3 meV, a factor of 2 larger than deduced from the RRS dynamics, and also too large to explain the SE spectrum. This mismatch is due to the fact that if only the top interface is growth interrupted, the noninterrupted interface shows a correlation to the monolayer formation on the top interface, leading to an effective thickness variation smaller than an integer monolayer, as it was observed in Ref. 3. The monolayer island size ξ_{ml} is also in agreement with the analysis of emission spectra of a series of growth-interrupted samples.³

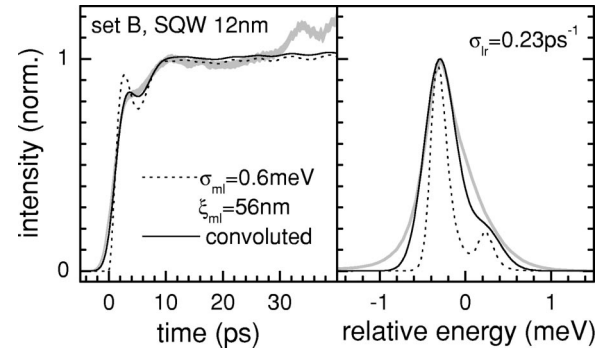


FIG. 15. Left: Comparison of the measured RRS dynamics of the 12-nm SQW of set B (gray shaded region) with the one calculated for a monolayer disorder with parameters as given (dotted line), and convoluted with the experimental time resolution (solid line). Right: Measured SE intensity spectra (gray solid line), compared with the calculated RRS spectra without long-range disorder (dotted line) and with long-range disorder (solid line) of variance σ_{lr} , as indicated.

To summarize the experimental results, we find that in the investigated series of samples, signatures of correlated level statistics are found in all SQW's, and explained within the model of excitons in a disorder potential. No strong initial oscillations, which are predicted for potential correlation lengths between about 30 nm and 200 nm, are found. Instead, the presence of a long-range part of the disorder with a correlation length in the micrometer range is suggested, which is increasing the RRS spectral width, while not altering the RRS dynamics for large scattering wave vectors.

V. CONCLUSION

In conclusion, we want to emphasize the following points.

(i) A large speckle average is important to overcome artifacts due to the statistical nature of the coherent SE over the direction. The relative statistical error is found to be $1/(\sqrt{N_{\text{eff}} n})$, giving a lower limit for the ensemble size needed to avoid random features in experimental results.

(ii) In the investigated series of single quantum wells, effects of correlations in the exciton level statistics are found as deviations from the dynamics of an ensemble of uncorrelated levels. They manifest as a reduction of the RRS intensity at early times, and depend systematically on the structural parameters.

(iii) A RRS dynamics slower than that expected from the RRS spectra is found in some samples, and attributed to a part of the disorder potential with a long correlation length in the micrometer range.

(iv) Using a disorder potential containing both monolayer steps of long correlation length and a Gaussian potential of short correlation length to simulate SQW's grown with growth interruption, the transition from the level-repulsion-dominated response to the oscillations with the monolayer-splitting frequency was investigated.

Further development of the theory in the direction of more realistic disorder correlation functions and including

the radiative coupling is desirable. On the experimental side the characterization of the disorder potential with independent methods such as cross-sectional scanning tunneling microscopy³² or selective etching³³ is needed for a quantitative comparison with the theoretical predictions, together with the design of samples spanning a larger range of disorder correlation lengths.

ACKNOWLEDGMENTS

Financial support by the DFG-Schwerpunktprogramm “Quantenkohärenz in Halbleitern” and by the European Union through Grant No. MCFI-1999-00728 for V. S. is acknowledged. The authors want to thank E. Runge for fruitful discussions.

-
- ¹J. Hegarty, M.D. Sturge, C. Weisbuch, A.C. Gossard, and W. Wiegmann, *Phys. Rev. Lett.* **49**, 930 (1982).
- ²C.A. Warwick, W.Y. Jan, A. Ourmazd, and T.D. Harris, *Appl. Phys. Lett.* **56**, 2666 (1990).
- ³K. Leosson, J.R. Jensen, W. Langbein, and J.M. Hvam, *Phys. Rev. B* **61**, 10 322 (2000).
- ⁴H. Stolz, D. Schwarze, W. von der Osten, and G. Weimann, *Phys. Rev. B* **47**, 9669 (1993).
- ⁵H. Wang, J. Shah, T. Damen, and L. Pfeiffer, *Phys. Rev. Lett.* **74**, 3065 (1995).
- ⁶R. Zimmermann, *Nuovo Cimento Soc. Ital. Fis., D* **17D**, 1801 (1995).
- ⁷D.S. Citrin, *Phys. Rev. B* **54**, 14 572 (1996).
- ⁸N. Garro, L. Pugh, R.T. Phillips, V. Drouot, M.Y. Simmons, B. Kardynal, and D.A. Ritchie, *Phys. Rev. B* **55**, 13 752 (1997).
- ⁹M. Gurioli, F. Bogani, S. Ceccherini, and M. Colocci, *Phys. Rev. Lett.* **78**, 3205 (1997).
- ¹⁰S. Haacke, R. Taylor, R. Zimmermann, I. Bar-Joseph, and B. Deveaud, *Phys. Rev. Lett.* **78**, 2228 (1997).
- ¹¹M. Wörner and J. Shah, *Phys. Rev. Lett.* **81**, 4208 (1998).
- ¹²W. Langbein and J.M. Hvam, *Phys. Status Solidi A* **178**, 13 (2000).
- ¹³W. Langbein and J.M. Hvam, *Phys. Rev. B* **61**, 1692 (2000).
- ¹⁴E. Runge and R. Zimmermann, in *Advances in Solid-State Physics*, edited by B. Kramer (Vieweg, Braunschweig, 1999), Vol. 39, pp. 423–432.
- ¹⁵D. Birkedal and J. Shah, *Phys. Rev. Lett.* **81**, 2372 (1998).
- ¹⁶G. Malpuech, A. Kavokin, W. Langbein, and J.M. Hvam, *Phys. Rev. Lett.* **85**, 650 (2000).
- ¹⁷J.P. Prineas, J. Shah, B. Grote, C. Ell, G. Khitrova, H.M. Gibbs, and S.W. Koch, *Phys. Rev. Lett.* **85**, 3041 (2000).
- ¹⁸V. Savona and R. Zimmermann, *Phys. Rev. B* **60**, 4928 (1999).
- ¹⁹V. Savona, S. Haacke, and B. Deveaud, *Phys. Rev. Lett.* **84**, 183 (2000).
- ²⁰F. Intonti, V. Emiliani, C. Lienau, T. Elsaesser, V. Savona, E. Runge, R. Zimmermann, R. Nötzel, and K.H. Ploog, *Phys. Rev. Lett.* **87**, 076801 (2001).
- ²¹K. Brunner, G. Abstreiter, G. Böhm, G. Tränkle, and G. Weimann, *Appl. Phys. Lett.* **64**, 3320 (1994).
- ²²W. Langbein, J.M. Hvam, and R. Zimmermann, *Phys. Rev. Lett.* **82**, 1040 (1999).
- ²³G. Kocherscheidt, W. Langbein, G. Mannarini, and R. Zimmermann, *Phys. Rev. B* **66**, 161314(R) (2002).
- ²⁴R. Zimmermann, F. Große, and E. Runge, *Pure & Appl. Chem.* **69**, 1179 (1997).
- ²⁵W. Langbein, K. Leosson, J.R. Jensen, J.M. Hvam, and R. Zimmermann, *Phys. Rev. B* **61**, R10 555 (2000).
- ²⁶E. Runge and R. Zimmermann, *Phys. Rev. B* **61**, 4786 (2000).
- ²⁷ N_{eff} can be derived from the second moment Q and the third moment S of the distribution via the relation $N_{\text{eff}} = 4Q^3/S^2$.
- ²⁸R. Zimmermann, E. Runge, and V. Savona, in *Quantum Coherence, Correlation and Decoherence in Semiconductor Nanostructures*, edited by T. Takagahara (Elsevier Science, Oxford, 2002).
- ²⁹W. Langbein, E. Runge, V. Savona, and R. Zimmermann, *Phys. Rev. Lett.* **89**, 157401 (2002).
- ³⁰Y. Yayon, A. Esser, M. Rappaport, V. Umansky, H. Shtrikman, and I. Bar-Joseph, *Phys. Rev. Lett.* **89**, 157402 (2002).
- ³¹H. Castella and J.W. Wilkins, *Phys. Rev. B* **58**, 16 186 (1998).
- ³²A.J. Heinrich, M. Wenderoth, K.J. Engel, T.C.G. Reusch, K. Sautthoff, R.G. Ulbrich, E.R. Weber, and K. Uchida, *Phys. Rev. B* **59**, 10 296 (1999).
- ³³G. Bernatz, S. Nau, R. Rettig, H. Jänsch, and W. Stolz, *J. Appl. Phys.* **86**, 6752 (1999).